Non-uniform distribution of myosin-mediated forces governs red blood cell curvature through tension modulation

H. Alimohamadi[1], A. S. Smith[2], V. M. Fowler[2,3] and P. Rangamani [*1]

[1]Department of Mechanical and Aerospace Engineering, University of California San Diego, CA 92093, USA
[2]Department of Molecular Medicine, The Scripps Research Institute, La Jolla, CA 92093, USA
[3]Department of the biological science, University of Delaware, Newark, DE 19716, USA

June 11, 2019

Abstract The biconcave disk shape of the mammalian red blood cell (RBC) is unique to the RBC and is vital for its circulatory function. Recent experiments have demonstrated that the biconcave shape of the RBC relies not only on the physical properties of the membrane but also depends on the molecular constituents of the membrane cytoskeleton, including the contractile activity of the nonmuscle myosin IIA (NMIIA) motor protein. Here, we use the classical Helfrich model for the RBC membrane and incorporate heterogeneous force distributions along the membrane to mimic the contractile activity of NMIIA. We find that the biconcave shape of the RBC depends on the ratio of forces per unit volume in the dimple and donut regions of the RBC. Experimental measurements of NMIIA densities at the dimple and donut validate our prediction that (a) membrane forces must be non-uniform along the RBC membrane and (b) the force density must be larger in the dimple region than the donut region to produce the observed membrane curvatures. Furthermore, we find that the tension of the RBC membrane plays an important role in regulating this force-shape landscape. Our findings of heterogeneous force distributions on the plasma membrane for RBC shape maintenance have implications for shape maintenance of many cell types.

Keyword Erythrocyte, Membrane curvature, Lipid bilayer, Actomyosin, Helfrich energy.

1-Introduction

Cell shape and function are intricately coupled; cells must maintain specific shapes to migrate, divide normally, support tissue and organ function [1, 2]. Maintenance or modification of cell shape is a concerted action of the actomyosin network at the whole cell level that allows for a stable actin network in polarized cells or a rapidly remodeling actin network for cell spreading and motility [3, 4]. Thus, networks of actin filaments (F-actin) and the F-actin-activated motor protein non-muscle myosin II (NMII) specify cell shape by exerting force on the plasma membrane to control membrane tension and curvature [5–8]. Disruption of these actomyosin networks can lead to dysregulation of cell shape and has been implicated in cancer [9–11], congenital hemolytic anemias [12–14], and neurodegeneration [15]. Local, nanoscale changes in actomyosin organization can lead to micron-scale changes in cell shape to support normal cell function [16].

Human red blood cells (RBCs) have a biconcave disk shape, with a central, narrow, dimple region surrounded by a thicker donut rim [13] (Fig. 1). This shape enables efficient gas and ion exchange and increases RBC deformability and resiliency in the circulation [17–19]. Deviations from biconcavity interfere with RBC function in diseases such as congenital hemolytic anemias [12], sickle cell disease [20], and malaria [21, 22]. Historically, the biconcave disk shape of the RBC has been modeled as a thin elastic shell using the Helfrich-Canham energy model [23, 24], treating the RBC as a lipid bilayer. This model, a classic in the field of membrane mechanics, was

---

*prangamani@ucsd.edu

1

able to explain the observed shape of the RBCs as a one-parameter family of solutions. The biconcave shape is obtained as the minimum energy configuration in response to a specified reduced volume or asymmetry between the membrane leaflets (termed spontaneous curvature) assuming homogeneous membrane properties across the entire surface [23–25].

However, the discovery of the molecular constituents of the RBC cytoskeleton has made it clear that the RBC membrane is not simply a lipid bilayer. It is now known that the biconcave morphology of an RBC is supported by a 2D quasi-hexagonal lattice of short (~ 37 nm) actin filaments interconnected by long (~ 200 nm), flexible $(\alpha_1\beta_1)_2$-spectrin heterotetramers [26–28]. The spectrin-F-actin membrane skeleton binds to membrane proteins to maintain membrane tension, curvature, and mechanical properties of the RBC [17, 18, 27–29]. In addition to the spectrin-actin network, RBCs contain NMII (predominantly the NMIIA isoform), with biochemical properties similar to NMII isolated from other cell types [30, 31]. Our recent study [32] demonstrates that in intact RBCs, NMIIA molecules assemble into bipolar filaments with F-actin-binding motor domains at either end and that NMIIA motor activity exerts forces on membrane skeleton F-actin to control RBC membrane tension, biconcave disk shape and deformability (Fig. 1A). These NMIIA filaments are sparsely distributed along the RBC membrane (~ 0.5 filaments per square micrometer) [32] and thus would be expected to apply localized forces to the membrane and skeleton, but this has not been tested.

In this study, we investigated the role of heterogeneous forces in modulating the shape of the RBC. We revisit the classical Helfrich model and modify it to account for localized forces to represent the NMIIA-generated forces on the plasma membrane. We test uniformly applied forces and a range of heterogeneously applied forces to determine the set of distributions that most closely reproduce experimentally observed RBC shapes. Our model predicts that the best match between simulations and experiments for RBC shapes is obtained when there are two curvature-dependent force domains – a dimple region with negative curvature and greater forces at the center of the RBC and a donut region with positive curvature and lower forces at the periphery (Fig. 1B). Experimental measurements of the NMIIA distribution validated our prediction of non-uniform force distribution; more NMIIA puncta are found in the dimple region than in the donut. Our model also predicts that membrane tension is a key determinant of the forces required in the dimple and donut regions, providing a potential design principle for RBC shape maintenance despite variations in NMIIA puncta localizations.

2-Model development

The RBC membrane is a thin elastic material that can bend but resists stretching. This feature enables the RBC to deform and adjust its shape in response to applied stresses. Here, we outline the governing equations of our model. This approach will allow us to predict how the induced surface forces by NMIIA motor activity can regulate the biconcave morphology of RBCs in mechanical equilibrium. To develop our model and solve it numerically, we make some assumptions as listed below.

2-1-Assumptions

- We consider that the curvature of the membrane is much larger than the thickness of the bilayer [25]. This allows us to treat the lipid bilayer as a thin elastic shell and model the bending energy of the membrane by the Helfrich–Canham energy, which depends only on the local curvatures of the surface [23, 24].

- Due to the high stretching modulus of lipid bilayers, we assume that the membrane is locally incompressible/inextensible [33]. We use a Lagrange multiplier to implement this constraint [34–36].

- We assume that the applied force by the NMIIA motor proteins is local and it is primarily normal to the membrane (see Fig. 1A) [37, 38]. The tangential contributions from the NMIIA-mediated forces are assumed to be negligible. This assumption can be justified based on the preferably orthogonal orientation of the short actin filaments to the erythrocyte membrane in the resting condition [39, 40].

- We assume that the RBC is at mechanical equilibrium at all time scales, allowing us to neglect inertia [41–43]. This assumption is consistent with the experimentally observed shapes for the resting RBCs in both *vivo* and *vitro* [37, 44].
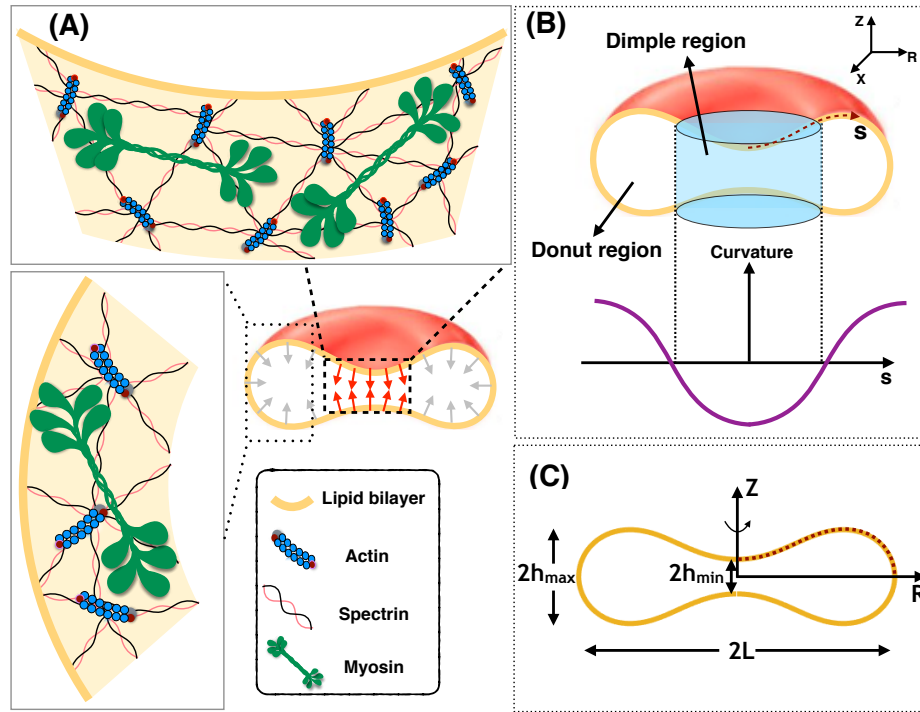
Figure 1: Interaction of the membrane and cytoskeleton controls the shape of the RBC. (A) Schematic depiction of the biconcave disk shape of an RBC plasma membrane and the cytoskeleton underneath. The effect of NMIIA filaments (shown in green) is modeled by local forces applied to the plasma membrane (red and gray arrows). (B) Two distinct regions are identified in a biconcave RBC – the dimple region and the donut region. In the dimple region (blue cylinder), each RZ cross-section of the shape has a negative curvature along its arclength. In contrast, in the donut, the curvature of each RZ section is positive along the arclength. (C) The geometry of a simulated RBC in axisymmetric coordinates and the three characteristic length scales that represent the biconcave shape of the RBC. $2h_{\min}$ is the minimum height at the dimple, $2h_{\max}$ is the maximum height at the rim, and $2L$ denotes the cell's maximum diameter. The dotted red curve shows the computational domain for our mechanical model.

- We assume that the total surface area of the RBC membrane is constant ($\sim$135 μm^2) [45, 46].

- For simplicity in the numerical simulations, we assume that the RBC is rotationally symmetric and also has a reflection symmetry with respect to the $Z = 0$ plane (see Fig. 1C) [24, 45, 47, 48]. This assumption reduces the computational cost of the simulation into just one curve as shown by the red dotted line in Fig. 1C.

2-2- Membrane mechanics

In mechanical equilibrium, the RBC shapes can be obtained as the result of minimization of the membrane bending energy including the applied forces by the cytoskeleton and the given physical constraints such as a local surface incompressibility condition. Here, to model the bending energy of the membrane, we use the Helfrich-Canham energy, defined by [23, 24, 34, 49–51],

$$W(H, K, \theta^\alpha) = \kappa H(\theta^\alpha)^2 + \kappa_G K(\theta^\alpha), \qquad (1)$$

where W is the energy density per unit area, θ^α denotes the surface coordinate where $\alpha \in \{1, 2\}$, $H(\theta^\alpha)$ is the local mean curvature, and $K(\theta^\alpha)$ is the local Gaussian curvature. κ and κ_G are constants representing the bending and Gaussian moduli respectively [52]. To minimize the bending energy (Eq. 1) and obtain the RBC shapes from simulations under the action of local forces, we used the variational approach which yields the so-called "shape equation" [49, 50],

$$\underbrace{\Delta[\kappa H] + 2\kappa H(H^2 - K)}_{\text{Elastic effects}} = \underbrace{p + 2\lambda H}_{\text{Capillary effects}} + \underbrace{F}_{\substack{\text{Force due} \\ \text{to skeleton}}} , \tag{2}$$

where Δ is the surface Laplacian (also known as the Beltrami operator), p is the pressure difference across the membrane, λ is the membrane tension, and F is the force density (force per unit area) representing the normally applied force density to the membrane surface by the NMIIA motor proteins. The shape equation (Eq. 2) basically represents the relationship between the forces applied by NMIIA motor proteins and the resulting shape of RBCs. A complete derivation of the governing equations of the motion, the notations used, and the non-dimensionalization procedure are presented in the supplementary online material (SOM).

2-3- Parametrization of RBC biconcave morphology and shape error estimation

The geometry of human RBCs has been studied extensively using a variety of different methods such as light microscopy [53, 54] , interference holography [55, 56], resistive pulse spectroscopy [57], micropipette aspiration [58, 59], and light scattering [60, 61]. In Fig. 2A, we summarize the reported values for the RBC geometrical parameters from the literature [53, 55, 58, 61–63], in terms of the three characteristic lengths (h_{min} , h_{max} and L) (Fig. 1C), the volume (V), the surface area (A), and the sphericity index (SI).

During the last few decades, several parametric models have been proposed to describe the biconcave morphology of the RBC [55, 56, 64–68]. Funaki proposed the Cassini oval model with two coefficients to represent the RBC geometry [64]. Kuchel et al. [65] and later Yurkin [66] modified the Cassini oval model to implicit equations with three and four coefficients, respectively. Borovoi et al. introduced a function in spherical coordinates to characterize the RBC morphology [67]. The most realistic model was proposed by Evans and Fung [55], where they first obtained images from 50 human RBC samples using light microscopy and then fitted a parametric equation to the RZ cross-sectional shape of the RBCs (Fig. 1C) using statistical analysis. The Evans and Fung proposed function is given by

$$Z(R) = \pm 0.5\sqrt{1 - (\frac{2R}{L})^2}(0.81 + 7.83(\frac{2R}{L})^2 - 4.39(\frac{2R}{L})^4) \tag{3}$$

where R is the radius from the axis of rotation and Z is the height from the base plane. In Fig. 2B, we plotted the different proposed parametric models for the biconcave shape of an RBC. We observed that for the fixed height of the dimple ($2h_{min}$), height of the rim ($2h_{max}$), and the maximum diameter (2L), all models generate similar shapes, but with slight differences. In this study, we used the Evans and Fung parametric equation in Eq. 3 as the reference data for the experimental shape of an RBC, since Eq. 3 was developed based on direct experimental measurement and fit well with the observed RBC shapes [69, 70].

To quantify the deviation between simulated geometries obtained from our mechanical model and the parametric shape equation (Eq. 3) for the RBC, we define three errors ϵ_{hmin}, ϵ_{hmax} and ϵ_L as

$$
\begin{aligned}
\epsilon_{hmax} &= |h_{max,par} - h_{max,sim}| = |\Delta h_{max}| \\
\epsilon_{hmin} &= |h_{min,par} - h_{min,sim}| = |\Delta h_{min}| \\
\epsilon_L &= |L_{par} - L_{sim}|| = |\Delta L|,
\end{aligned}
\tag{4}
$$

where $(.)_{,par}$ is the experimentally measured length scale fitted to the parametric equation (Eq. 3) and $(.)_{,sim}$ is the length scale obtained from the numerical simulation (Eq. 2). The total error (ϵ_{total}) in the shape of the simulated RBCs is then calculated by the root mean square (RMS) between every two mapped points in the parametric shape of an RBC and the simulated geometries (Fig. 2C) given by

$$\epsilon_{total} = \sqrt{\frac{1}{N}[\sum_{i=1}^{i=N}(Z_{i,sim} - Z_{i,par})^2 + (R_{i,sim} - R_{i,par})^2]} \tag{5}$$

4

(A)

Reference	2L (μm)	2h$_{min}$ (μm)	2h$_{max}$ (μm)	V (μm^3)	A (μm^2)	SI (4.83(V)$^{2/3}$/A)
Canham et al. [53]	8.07 $\pm$ 0.55			107 $\pm$ 18.8	138 $\pm$ 17.4	0.783
Evans et al. [55]	7.82 $\pm$ 0.62	0.81 $\pm$ 0.35	2.58 $\pm$ 0.27	94 $\pm$ 14	135 $\pm$ 17	0.742
Linderkamp et al. [58]	7.9 $\pm$ 0.4	1.84 $\pm$ 0.13		90.5 $\pm$ 4.4	137 $\pm$ 6.7	
Tarasov et al. [61]				87 $\pm$ 20	135 $\pm$ 28	
Ergul et al. [62]	7.7			80.9		
Das et al. [63]	9.52 $\pm$ 0.56					
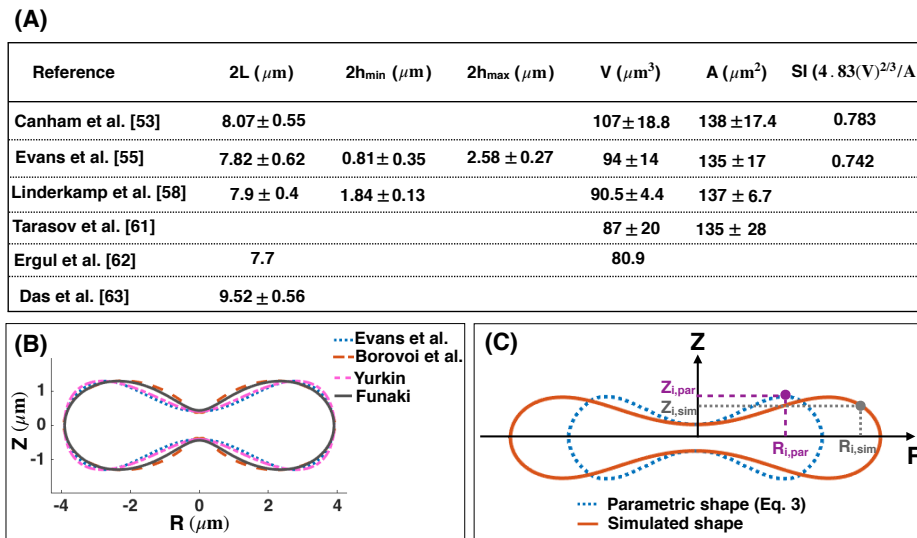
Figure 2: (A) Healthy human RBC dimensions from the literature [53, 55, 58, 61–63]. (B) Comparison between the proposed parametric models describing the biconcave morphology of an RBC. There is a close match between the four models for the fixed minimum height of the dimple, maximum height of the rim, and the maximum diameter. (C) Discretization scheme of the parametric shape of an RBC (Eq. 3) (dotted blue line) and the simulated geometry obtained from our mechanical model (Eq. 2) (solid red line). Each experimental and simulated shape is discretized into N nodes where i indicates the node index. These nodes are used to compute the total error in the simulated RBC geometry (Eq. 5).

where N is the total number of nodes across the RBC shapes, i is the index node, $Z_{i,\text{sim}}$ and $Z_{i,\text{par}}$ are the height of the simulated and the parametric (Eq. 3) RBC shape at index i, respectively. $R_{i,\text{sim}}$ is the radius of the simulated shape at index i, and $R_{i,\text{par}}$ is the radius of the RBC parametric shape (Eq. 3) at index i.

While Eq. 5 represents the error in the simulated shapes compared to the RBC parametric shape, it does not capture the measurement errors since Eq. 3 was developed based on the average dimensions of experimentally observed RBCs. However, there are standard deviations in the measured dimensions as reported by Evans and Fung [55], and also the microscopy images are noisy, making it difficult to extract the exact shape of the membrane without uncertainty. Here, to account for these uncertainties, we assume that the given parametric equation by Evans and Fung [55] can be written as

$$Z(R) = Z_{\text{mean}}(R) + Z_{\text{error}}(R) \tag{6}$$

where $Z_{\text{mean}}(R)$ is the given function in Eq. 3 and we define $Z_{\text{error}}(R)$ as the fitting error of the Evans and Fung parametric equation to the actual shape of an RBC. In this study, we assume that $Z_{\text{error}}(R)$ is 10% of the $Z_{\text{mean}}(R)$ in order to represent the variance of RBC dimensions.

2-4-Numerical implementation

Simplifying the shape equation (Eq. 2) for a rotationally symmetric RBC gives us a set of first order differential equations (Eq. S9). In order to obtain the RBC shapes from simulation and determine the role of NMIIA-generated forces in maintaining the biconcave morphology, we need to solve the coupled differential equations (Eq. S10) along with the defined boundary conditions (Eq. S10). Here, we used the commercially available finite element solver COMSOL MULTIPHYSICS 5.3a to solve the governing differential equations (Eqs. S9 and S10). In all our simulations, the transmembrane pressure is set to zero (p=0).

5

3- Results

3-1- Uniform distribution of force density across the membrane surface is not sufficient to recover the biconcave shape of an RBC

Modeling studies of RBC shapes have been based on the assumption that the RBC membrane and cytoskeleton are spatially homogeneous [17, 18, 27, 52]. In this study, we aimed to incorporate the effect of NMIIA on the RBC membrane and therefore modeled the interactions between the membrane and NMIIA as a local force applied on the membrane. We first performed simulations applying a uniform pulling force density ($F_{uniform}$) across the cell membrane surface (Figs 3A, B). This uniform pulling force density can be interpreted as a pressure difference between the inside and outside of the RBC which specifies the change in the RBC volume compared to an equivalent sphere (known as the reduced volume) [25, 71, 72]. Considering the RBC membrane rigidity and elasticity, experimental measurements showed that a small pressure difference – on order of $\sim 1 \, pN/\mu m^2$ – is sufficient to form and maintain a biconcave RBC from a spherical cell [72–75].

To perform our simulations, we assumed that the RBC membrane area is large enough that the lateral membrane tension is negligible ($\lambda = 0$) [76–78]. We also set the bending modulus to be in the range of physiologically reported values for the RBC membrane ($\kappa = 9 \times 10^{-19}$J) [77]. As shown in Fig. 3C, for a given value of uniform pulling force, we were able to match two out of three characteristic length scales of the simulated shapes with the parametric shape of an experimentally observed RBC (Eq. 3). Furthermore, we can see that for all configurations in Fig. 3C, the calculated uniform force density from our mechanical model is in the range of the reported pressure difference for a biconcave RBC ($F_{uniform} \sim 1 \, pN/\mu m^2$), which validates the accuracy of our numerical results (Fig. 3C, bottom row).

Based on the results in Fig. 3C, we observe that for the large value of the pulling force density ($F_{uniform} \sim 1.88 = pN/\mu m^2$) the maximum and the minimum heights of the simulated shape match well with the parametric shape, while the maximum diameter does not (Fig. 3C left). For the intermediate pulling force density ($F_{uniform} \sim 1.81 = pN/\mu m^2$), the minimum height and the maximum diameter of the simulated shape are in good agreement with the parametric shape, but the maximum height is not (Fig. 3C center). Finally, for the small pulling force density ($F_{uniform} \sim 1.02 = pN/\mu m^2$), the mismatch between the simulated geometry and the parametric shape of the RBC is in the minimum height of the dimple (Fig. 3C right).

For each value of the applied pulling force density, we plotted the error for each of the characteristic lengths (L, h_{max} or h_{min}) (Eq. 4) and the total error (Eq. 5) (Fig. 3C). We found that both the characteristic and the total shape errors have the lowest value ($\epsilon_{hmax} \sim 0.4 \, \mu m$ and $\epsilon_{total} \sim 0.32 \, \mu m$) at the intermediate uniform force density, when there is only a relatively small mismatch in the maximum height (Δh_{max}) (Fig. 3C center). Thus, we can predict that among the three main characteristic length scales of an RBC, the maximum height of the rim (h_{max}) appears to be the least critical dimension in order to minimize the shape error of the simulated geometries. It should be mentioned that for each case here, we first calculated the mean errors based on the given parametric equation (Eq. 3) and then we computed the error bars using Eq. 6.

3-2- Local force density at the RBC dimple reduces the shape error

Given that the shape mismatch even for the intermediate uniform force density is relatively large compared to the described RBC dimensions in Fig. 2, we next asked if we could change the distribution of the non-uniform pulling force density to reduce the shape error and obtain a better agreement between the experimentally reported shapes for RBCs and our model. We conducted simulations of Eqs (S10) and (S11) but this time assuming that the applied force per unit area is locally concentrated in the dimple region (F_{dimple}), and that there is no force along the surface of the donut region (Figs 4A, B). This heterogeneous force distribution along the membrane was implemented using a hyperbolic tangent function (Eq. S21).

In Fig. 4C, we compare the RBC shapes obtained from the simulation with the application of increasing local pulling force density at the dimple. We find that the total error is a nonlinear function of the F_{dimple}; as F_{dimple} increases, the total error in shape mismatch decreases and then increases again. Based on the shape of the simulated RBC, we can identify three different regimes (Fig. 4C). For low dimple force density (($F_{dimple} < 1.81 \, pN/\mu m^2$), the simulated geometry has a spherical shape ($h_{max} = h_{min}$) and therefore the shape error is large ($\epsilon_{total} > 2 \, \mu m$, yellow
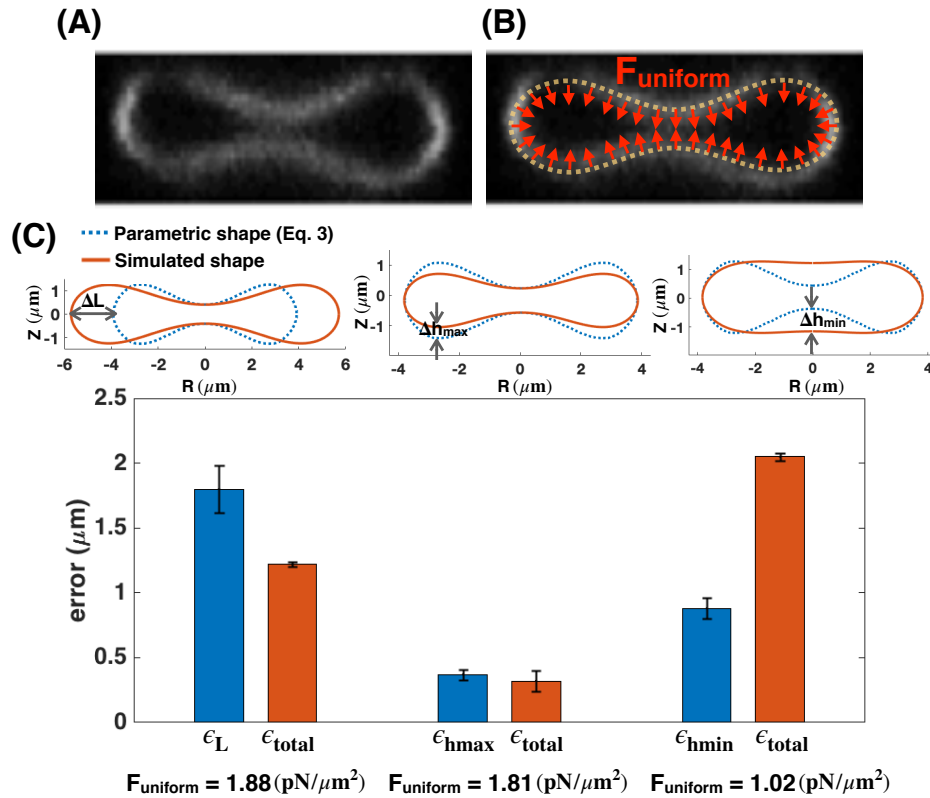
6

Figure 3: Mismatch between the parametric shape of an experimentally observed RBC (Eq. 3) and the shapes obtained from simulations (Eqs. S10) with a uniform distribution of the pulling force density across the membrane surface. (A) RZ view of the center of an RBC from a confocal Z-stack of an RBC stained for the membrane marker glycophorin A. (B) Schematic of a biconcave RBC with a uniform distribution of the normal pulling force density (red arrows). $F_{uniform}$ represents the magnitude of the pulling force density. (C) Calculated error in the characteristic length scales (Eq. 4) and total shape error (Eq. 5) for different values of the force density. In each case, two out of three main length scales of the simulated geometries are matched closely to the parametric shape of an RBC. The total shape error (ϵ_{total}) calculated by Eq. 5 is minimum for $F_{uniform} = 1.81 \ \mathrm{pN}/\mu\mathrm{m}^2$, when there is only a mismatch in the maximum height of the RBC morphology (center bar).

area in Fig. 4C). By increasing the magnitude of dimple force density ($1.81 \ \mathrm{pN}/\mu\mathrm{m}^2 < F_{dimple} < 3.73 \ \mathrm{pN}/\mu\mathrm{m}^2$) the dimple forms — biconcave shapes where $h_{max} > h_{min}$ — and the shape error decreases sharply (purple area in Fig. 4C). At higher levels of force applied at the dimple ($F_{dimple} > 3.73 \ \mathrm{pN}/\mu\mathrm{m}^2$, the error increases because the distance between the two bilayers in the dimple becomes too narrow (kissing shapes where $h_{min} \rightarrow 0$) (Fig. 4C).

Based on our results in Fig. 4C, the shape error has the minimum value of $\epsilon_{total} \sim 0.22 \ \mu\mathrm{m}$ for the case that $F_{dimple} = 3.73 \ \mathrm{pN}/\mu\mathrm{m}^2$ This total error is less than that for all the simulated shapes determined in the case of a uniform force applied to the membrane (Fig. 3C). We also observed a similar nonlinear trend in the calculated errors for the characteristic lengths (Eq. 4) as a function of dimple force density (Fig. S1). From these results, we conclude that there is a better match between the simulated shape and the parametric shape of an experimentally observed RBC when a localized force is applied at the RBC dimple compared to the case with a uniform force distribution (Fig. 3).

3-3- Non-uniform distribution of force density in the RBC dimple region versus the RBC donut region minimizes the shape error

While local force density at the dimple decreased the error in our simulated RBC shapes, NMIIA is known to be distributed throughout the RBC [32]. Therefore, we next asked if the shape error can be minimized by including a force at the donut region in addition to the applied force at the dimple region (Fig. 5A). This analysis will allow us
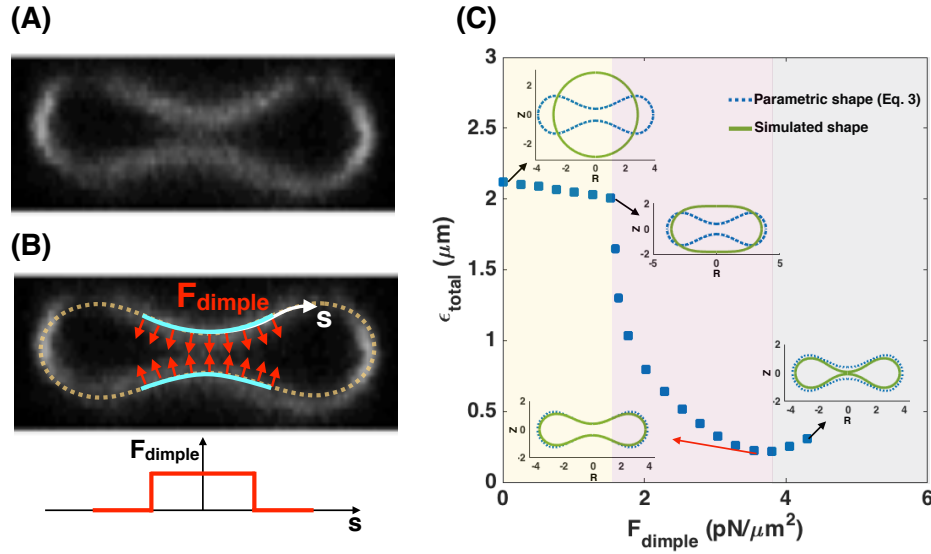
7

Figure 4: A local distribution of the pulling force density at the RBC dimple results in a better match between the parametric shape of an experimental observed RBC (Eq. 3) and the shape obtained from the simulation. (A) RZ view of the center of an RBC from a confocal Z-stack of an RBC stained for the membrane marker glycophorin A. (B, upper) A schematic depicting a biconcave RBC with a local force at the dimple area (red arrows) and no force in the donut region. F_{dimple} represents the magnitude of the pulling force density in the dimple region. (B, lower) The applied force density at the dimple as a function of the arclength (Eq. S21). (C) The simulated shape of the RBC with a local pulling force density in the dimple (solid green line) in comparison with the RBC parametric shape (dotted blue line). (C) The nonlinear behavior of the total error when increasing the dimple force density (F_{dimple}). Three different regimes can be identified based on the shape of the simulated RBC; (i) the spherical shapes where $h_{max} = h_{min}$ for the low F_{dimple} (yellow area), (ii) the biconcave shapes where the dimple forms ($h_{max} > h_{min}$) for the average F_{dimple} (purple area), and (iii) the kissing shapes where $h_{min} \to 0$ for large F_{dimple} (gray area). The shape error has the lowest value at $F_{dimple} = 3.73$ pN/μm^2 when the minimum height of the dimple in the simulated geometry matches closely with the minimum height of the parametric shape.

to predict the RBC shape not only in terms of absolute values of forces in the dimple and donut regions, but also as a function of force per unit volume ratio in these two regions. In our model, based on the given force density per unit area in the dimple (F_{dimple}) and donut (F_{donut}) regions, we define the ratio of forces per unit volume as

$$F_{ratio} = \frac{F_{dimple}}{F_{donut}} \times \frac{A_{dimple} \times V_{donut}}{A_{donut} \times V_{dimple}} \quad (7)$$

where A_{dimple} and A_{donut} are the area of the membrane surface in the dimple and donut regions, and V_{dimple} and V_{donut} are the volume occupied by the dimple and donut regions, respectively. For a given RBC shape, the area and the volume of the dimple and donut regions can be calculated by Eq. S11a and Eq. S11b, respectively.

We begin our analysis with the case that the pulling force in the dimple area is larger than the pulling force in the donut section ($F_{donut} < F_{dimple}$). We implemented this distribution of force along the RBC membrane via a hyperbolic tangent function (Eq. S21) and performed the simulations over a range of forces at the dimple and the donut regions ($F_{dimple} = 3.5$ - 14 pN/μm^2 and $F_{donut} = 0$ - 3.5 pN/μm^2. The range of dimple force (F_{dimple}) is chosen based on our previous results (Fig 4) to have a close comparison with the parametric shape and obtain biconcave shapes from simulations with $h_{max} > h_{min}$ and $h_{min} > 0$. The donut force (F_{dimple}) is set between $F_{donut} = 0$ and $F_{donut} = 3.5$ pN/μm^2 to impose the condition of $F_{ratio} < 1$ for all simulations.

The heat map in Fig. 5B represents the magnitude of the shape error for a given force density at the dimple and donut region. The simulations were stopped when the height at the RBC dimple tends to zero, shown as white domains in the heat map (Fig. 5B). Based on these calculations, we found that the shape error has the lowest value ($\epsilon_{total} \sim 0.16$ μm) when $F_{dimple} = 4.05$ pN/μm^2 and $F_{donut} = 0.28$ pN/μm^2 (the **X** point on the heat map). For

these specific force values, the parametric shape of the RBC (Eq. 3) and the shape obtained from the simulation at point ($\mathbf{X}$) are very well-matched (Fig. 5B lower panel).

To further understand the relationships between F_{donut} and F_{dimple} in governing the shape of the RBC, we plotted the shape error as the function of F_{dimple} for five different values of the force density at the donut section (Fig. 5C). We found that the shape error shows the same nonlinear dependence for different values of F_{donut}. By increasing the value of F_{dimple}, the shape error initially decreases by an order of magnitude and attains a relative minimum for each curve (Fig. 5C). Any further increase in the dimple force density results in a larger shape error (Fig. 5C), similar to Fig. 4B. As expected from Fig. 5B, the shape error has the lowest value on the red curve (F_{donut} = 0.28 pN/μm^2) when F_{dimple} = 4.05 pN/μm^2 Using Eq. 7, this set of dimple and donut forces in Fig. 5B is equivalent to $F_{ratio} \sim 16.24$, which reflects the prediction that to obtain the best match between the simulated RBC shape and the experimentally observed morphology, 16.24 times larger force per unit volume should be applied in the dimple region than the donut area.

Thus far, we have only considered the cases in which NMIIA motors were able to exert small pulling forces in the donut area. However, two other force configurations are possible; (i) NMIIA motors apply a larger force
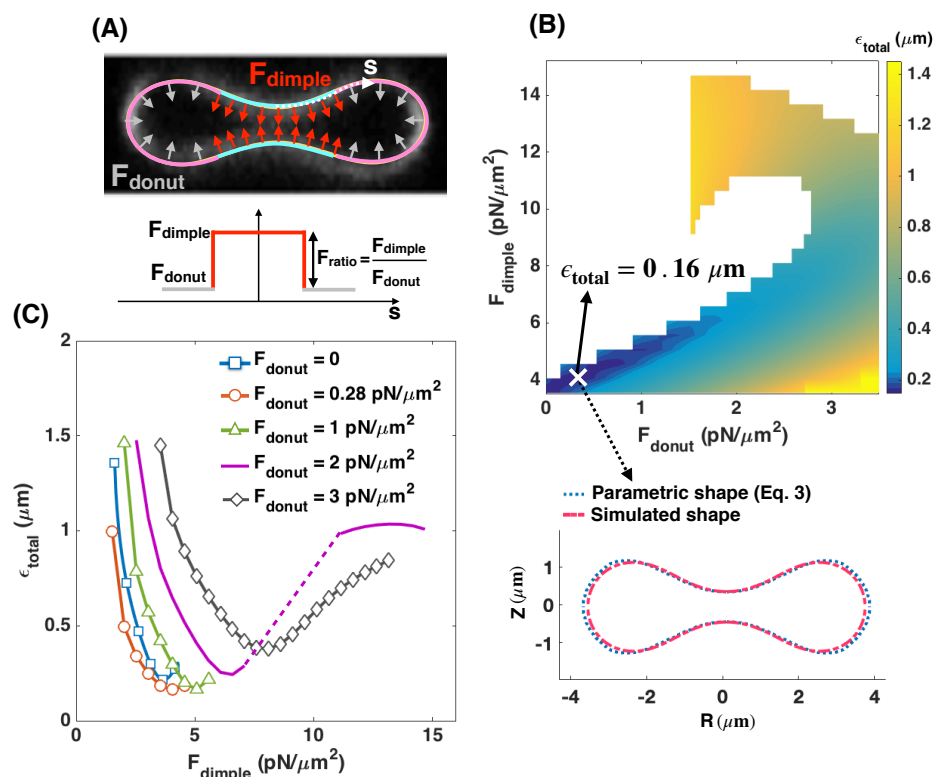

Figure 5: The applied force densities at the RBC dimple and donut regions regulate the shape error. (A, upper) Schematic of a biconcave RBC with a large force density (red arrows) at the dimple and a small force density (gray arrows) at the donut section. Schematic is overlaid on an RZ view of the center of an RBC from a confocal Z-stack of an RBC stained for the membrane marker glycophorin A. (A, lower) The applied force density along the membrane as a function of the arclength (Eq. S21). (B) Heat map shows the calculated shape error (Eq. 5) for a range of the force densities at the dimple (F_{dimple}) and donut (F_{donut}) regions. We stopped the simulations when the height at the dimple tends to zero ($h_{min} \rightarrow 0$). The marked point ($\mathbf{X}$) shows the case that has the lowest value of the error in the heat map at F_{dimple} = 4.05 pN/μm^2 and F_{donut} = 0.28 pN/μm^2. A comparison between the parametric shape of an RBC (dotted blue line) and the shape obtained from the simulation at point $\mathbf{X}$ (dashed red line) is shown in the lower panel. (C) The shape error as the function of force density at the dimple (F_{dimple}) for five different values of the applied force density at the donut area. The dotted purple line shows a discontinuous transition in the shape error by increasing the dimple force density for F_{donut} = 2 pN/μm^2. Similar to Fig. 4B, independent of the value of F_{donut}, the total error is a nonlinear function of the dimple force density (F_{dimple}).

9

density in the donut region than the dimple area ($F_{donut} > F_{dimple}$) (Fig. S2A), and (ii) NMIIA motors exert pushing forces in the donut region (Fig. S3A). We found that having a large pulling force in the donut region ($F_{donut} > F_{dimple}$) generates a shape resembling a peanut-shaped vesicle with a large shape error of $\epsilon_{total} \gg 1 \ \mu$m (Fig. S2). We also observed that applying a pushing force in the donut region ($F_{donut} = 3.73 \ pN/\mu m^2$ (no force in the dimple) causes a large error of $\epsilon_{total} \sim 0.46 \ \mu$m (Fig. S3B). Even adding a small pushing force in the donut area ($F_{donut} = 0.53 \ pN/\mu m^2$ with $F_{dimple} = 3.73 \ pN/\mu m^2$ increases the shape error to $\epsilon_{total} \sim 0.38 \ \mu$m (Fig. S3C). Our major prediction is that RBC biconcave shape depends on a heterogeneous distribution of NMIIA forces, which could be accomplished by more NMIIA motors in the dimple and less in the donut.

3-4- RBC dimple region has a higher concentration of NMIIA puncta compared to the donut region

Our simulations suggest that NMIIA-mediated force densities are not uniformly distributed across the RBC membrane but instead are larger in the dimple than the donut region (Fig. 5). Therefore, we hypothesized that the NMIIA distribution in RBCs is also non-uniform, with more NMIIA in the dimple region than the donut region. To test this hypothesis, we localized NMIIA motor domain puncta in three-dimensional reconstructions of AiryScan confocal Z-stacks [32, 79]. This assay detects myosin bipolar filaments and other higher-order structures, as individual NMIIA molecules are too dim to detect in AiryScan images.

We divided each RBC into dimple and donut regions based on F-actin staining at the membrane (Fig. 6A) and quantified the number of NMIIA motor domain puncta in each region and the volumes of each region and the RBC using Volocity software. The dimple region accounted for about 7.4% of the total RBC volume (based on the F-actin staining, Fig. 6B). This value agrees with calculations of dimple volume ($\sim 7.1\%$ of total volume) from our simulated shapes, in which we classify the dimple and donut regions based on the sign of the local mean curvature (Fig. 1B). The number of NMIIA puncta varies between RBCs, with 125 ± 47 puncta in the whole RBC, 113 ± 42 puncta in the donut, and 12 ± 9 puncta in the dimple (all values are mean $\pm$ SD). The dimple region contains about 9.1% of the total NMIIA motor domain puncta (Fig. 6C). In the dimple and donut regions as well as the whole RBC, the number of NMIIA puncta tends to increase with increasing region or cell volume (Fig. S4).

The number of NMIIA puncta per unit volume (μm^{-3}) in an RBC region is likely proportional to the number of NMIIA filaments that interact with membrane skeleton F-actin to exert force on the RBC membrane. The whole RBC and the donut region have similar NMIIA puncta densities ($1.73 \pm 0.562 \ \mu m^3$ and $1.70 \pm 0.556 \ \mu m^3$, respectively), while the dimple region has a $\sim 25\%$ higher density ($2.15 \pm 0.888 \ \mu m^3$ (Fig. 6D). Thus, the dimple region has ~ 1.29 times higher NMIIA puncta density compared to the donut region (Fig. 6E).

To determine whether differences in NMIIA densities relate to RBC biconcavity, we related NMIIA density to the minimum and maximum heights of XZ slices at the center of each RBC (Fig. S5). In both whole RBCs (Fig. S5A) and the dimple region (Fig. S5C), RBC biconcavity increased with increasing NMIIA density, while NMIIA density in the donut region was not related to biconcavity (Fig. S5B). These results agree with the results of our simulations, which predict that the maximum height of the rim (h_{max}) is the least critical dimension to minimize the shape error (Fig. 3) and furthermore, that NMIIA exerts a larger force density at the RBC dimple (Fig. 5). Together, our simulations and experimental data suggest that this non-uniform force distribution is required to specify RBC biconcave disk shape.

3-5- Effective membrane tension regulates the required force densities ratio in the RBC dimple versus the donut region

In Fig. 5, we found that for the simulated RBC shapes, the error is minimized when the applied force density in the dimple region is about 16.24 times larger than the donut area ($F_{ratio} = 16.24$), in a tensionless membrane. However, our experimental measurement reveals that in a healthy human RBC, the dimple region has only $\sim 25\%$ higher density of NMIIA puncta than the donut region (Fig. 6). If we assume that the NMIIA density is proportional to the force generation capacity, then the induced force in the dimple region should be 1.25 times larger than the donut area. Therefore, we set out to reconcile this apparent discrepancy in the predicted F_{ratio} and measured NMIIA density ratio. We found an interesting observation in the literature that the membrane tension in RBCs can vary from $10^{-1} \ pN/nm$ to $10^{-4} \ pN/nm$ [52, 77, 80]. Here, we interpret membrane tension to be the effective contribution of the membrane in-plane stresses and the membrane-cytoskeleton interactions [81]. We hypothesized
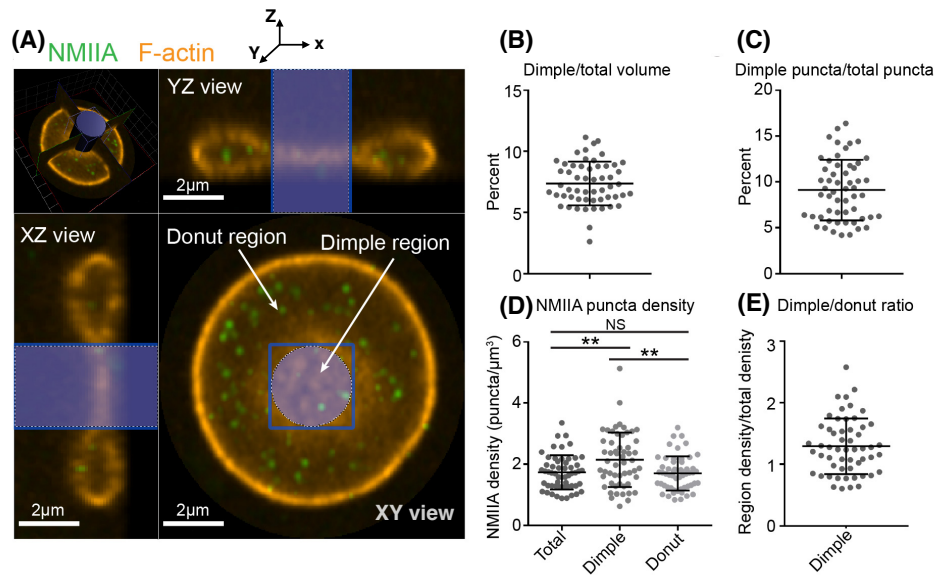
Figure 6: Figure 6: The RBC dimple has a higher average NMIIA puncta density than the RBC donut. (A) Optical section of a super-resolution Airyscan confocal Z-stack of human RBC immunostained with an antibody to the motor domain of NMIIA (green) and rhodamine-phalloidin for F-actin (orange). The top left image shows a perspective view of the optical section. Top right and bottom left images show YZ and XZ slices, respectively, of the RBC from planes perpendicular to this optical section. The bottom right image shows an XY view of the optical section. The blue cylinder represents the region identified as the dimple region. The rest of the RBC is identified as the donut region. (B) The percent of total RBC volume occupied by the dimple region. Mean±S.D. = 7.37±1.79. (C) The percent of total NMIIA puncta in the dimple region. Mean±S.D. = 9.11±3.30. (D) The RBC dimple region has a 25% higher density of NMIIA puncta than whole RBCs (Total) (p = 0.0051) or the donut region (p = 0.0023) by Tukey's multiple comparisons test. Mean±S.D.: Total = 1.73±0.562; Dimple = 2.15±0.888; Donut = 1.70±0.556. (E) Ratio of dimple and donut region NMIIA puncta densities for each RBC. Mean±S.D. = 1.29±0.452. (B-E) n = 55 RBCs from 3 individual donors.

that this in-plane tension of the RBC could play a critical role in relating the RBC shape and the NMIIA-generated force ratio in dimple and donut regions.

To investigate how this variation in membrane tension can modulate F_{ratio} and the shape error, we repeated the simulations as in Fig. 5 for three different effective membrane tensions: (i) low membrane tension (tension = 10^{-4} pN/nm) (Fig. 7A), (ii) intermediate membrane tension (tension = 10^{-3} pN/nm) (Fig. 7B), and (iii) high membrane tension (tension = 10^{-2} pN/nm) (Fig. 7C). The marker ($\mathbf{X}$) in each heat map shows the point with minimum shape error for that set of simulations. To visualize the geometry of the simulated RBC at each point marked with an '$\mathbf{X}$', we plot the shapes that were obtained from simulations (solid yellow line) versus the reference experimental data (dotted blue line) [55].

We observe that the shape error is almost constant ($\epsilon_{total} \sim 0.15$ μm) with increasing the membrane tension from zero to low and intermediate values (Fig. 7A, B). However, varying the membrane tension alters the force ratio that gives the minimum shape error. For example, at the low tension, the minimum shape error occurs at F_{ratio} = 3.88 and at the intermediate tension the shape error is minimum when F_{ratio} = 1.35 (Fig. 7A, B). In the case of the high membrane tension, we found that the simulated shape deviates significantly from the biconcave disk and becomes closer to pancake and the error goes up noticeably to about half a micrometer ($\epsilon_{total} \sim 0.5$ μm) (Fig. 7C).

Additionally, we found that for low and intermediate tension independent of the value of F_{donut}, the shape error has the same non-linear relationship with increasing F_{dimple} as observed before for the tensionless membrane (Fig. 7D, E). At the low tension, the minimum shape error occurs when F_{donut} = 5.04 pN/μm^2 and F_{donut} = 1.4 pN/μm^2 (blue square line) (Fig. 7D). At the intermediate tension, a combination of F_{donut} = 12.53 pN/μm^2 and F_{donut} = 10 pN/μm^2 gives the minimum shape error (green triangle line) (Fig. 7E). However, for high tension, because of the stiffness of the membrane, we observe not only a deviation from the biconcave shape but also a
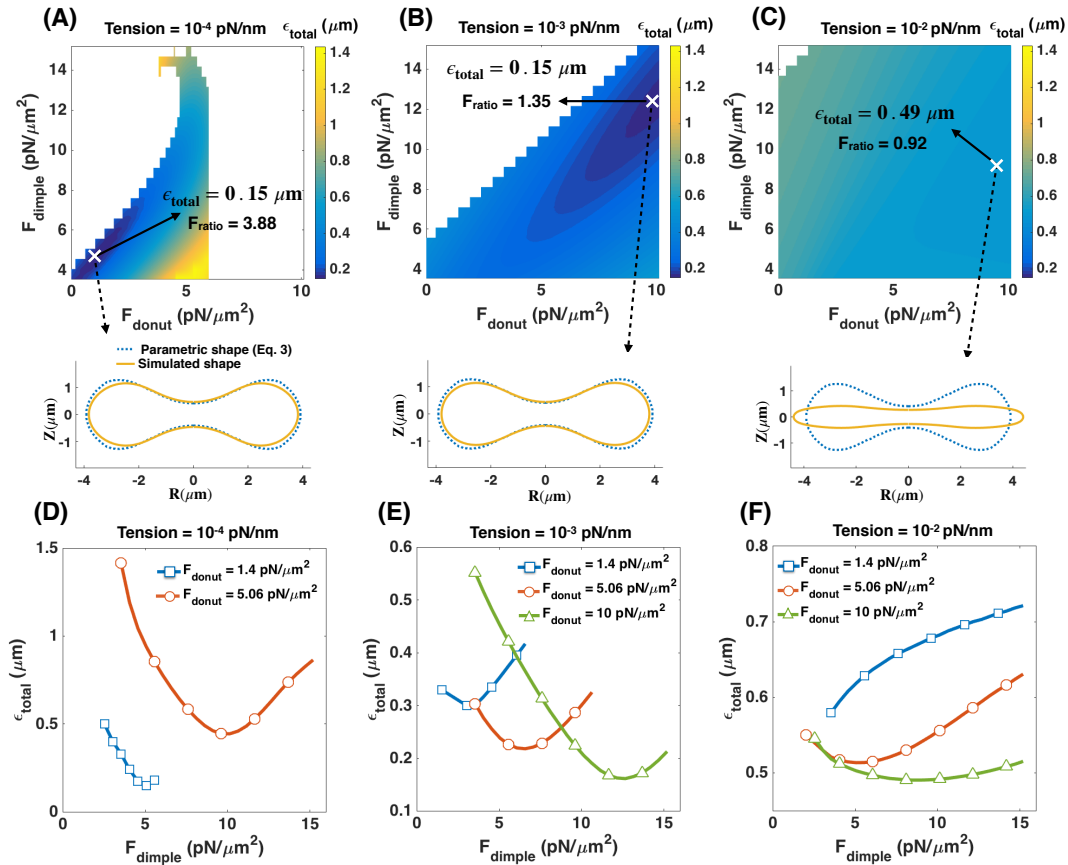
11

Figure 7: Effective membrane tension is a key parameter in regulating the RBC shape in addition to applied forces in the dimple and donut regions. (A-C) Heat maps show the total error in the shape of the simulated RBCs for (A) low tension (tension = 10^{-4} pN/nm), (B) intermediate tension (tension = 10^{-3} pN/nm), and (C) high tension (tension = 10^{-2} pN/nm). In each heat map, the point with the minimum error is marked with **X**. Also, for each marked point, the shape of the simulated RBC (solid yellow line) is shown in comparison with the reference experimental data in Eq. 3 (dotted blue line). At the intermediate tension, the shape error has the lowest value when $F_{ratio} = 1.35$ consistent with our experimental results in Fig. 6. (D-F) The calculated shape error (Eq. 5) as a function of the dimple force density (F_{dimple}) for different values of the donut force density and the membrane tension.

deviation from the nonlinear error - dimple force relationships (Fig. 7F).

Based on these results we can conclude that in addition to a non-uniform force distribution along the RBC membrane, a non-zero intermediate tension is required to obtain a close match between the shape of the simulated RBC and the experimental data. Furthermore, the intermediate value of tension (tension = 10^{-3} pN/nm) gives an excellent quantitative match for the predicted value of F_{ratio} (Fig. 7B) and the experimentally observed NMIIA density ratio (Fig. 6).

4- Discussion

The biconcave disk shape of mammalian RBCs provides a maximum surface-area-to-volume ratio, which enables efficient gas and ion exchange and increases RBC deformability and resiliency [82]. This shape has been studied extensively from a mechanical standpoint to identify stress-strain relationships in cell membranes. Most studies modeling RBC shapes have been based on the work of Canham and Helfrich [42, 47] and have reinforced the idea that mechanical force balance on the membrane by itself can provide a good insight into the unique shape of the RBC. Canham and Helfrich suggested that the minimization of the membrane bending energy, the asymmetry between the inner and outer membrane leaflets, and the osmotic pressure difference across the membrane generate

the RBC biconcavity [23–25].

In RBCs, the cytoskeleton underneath the plasma membrane is an elastic network of spectrin linked to short actin filament nodes and attached to the membrane by anchoring proteins [26]. Different studies have demonstrated the importance of membrane/cytoskeleton interaction in the formation of unusual RBC shapes and as well as the RBC deformability in shear flow [38, 83–86]. However, few theoretical models for RBC biconcave shape have considered an active role for the RBC cytoskeleton (e.g., the role of motors) in regulating RBC morphology [84, 87]. Studies of human and mouse congenital hemolytic anemias have established a role for the RBC cytoskeleton in maintaining the RBC biconcave shape in circulation [17, 18, 27]. Recently, Smith et al. [32] showed that active motor-dependent interactions of NMIIA with F-actin in the RBC cytoskeleton control RBC membrane tension and curvature to maintain the biconcave disk shape. Building upon the previous studies of mechanical force balances, here we have extended a membrane mechanics model to include non-uniform forces due to NMIIA-actin interactions.

There are two main conclusions that we can draw from our study. First, the density of the NMIIA-generated force must be non-uniform along the RBC membrane to produce the best fit with the shapes measured experimentally. By conducting a parameter sweep of the force density configurations, we found that the non-uniform force distribution must be such that F_{dimple} is larger than F_{donut} (Figs. 4, 5). Experimental measurements of NMIIA density in the dimple and donut regions of RBCs using immunofluorescence showed that indeed NMIIA density was higher in the dimple than in the donut (Fig. 6) by about 25%. Our combined computational and experimental results highlight that a non-uniform force distribution of NMIIA plays an important role in maintaining the biconcave shapes of RBCs.

Second, we found that the effective membrane tension is an important physical parameter in modulating the required NMIIA-mediated force density ratio in the RBC dimple versus the donut region (F_{ratio}) (Fig. 7). When compared to tensionless or low-tension membranes, the intermediate tension values F_{ratio} for minimum shape error (~ 1.35) match closely with the experimentally reported NMIIA density ratio at the dimple versus the donut. Furthermore, we found that varying the membrane tension to lower or higher values not only leads to deviation of the simulated shapes from the reference experimental data but also changes the required NMIIA force density ratio (Fig. 7).

Therefore, we predict that in mature, healthy biconcave RBCs, NMIIA motor domains exert force on a membrane under intermediate membrane tension ($\sim 10^{-2}$ pN/nm). The exact value of membrane tension in an intact RBC is hard to measure [88] because of the contributions from both the membrane and underlying cytoskeleton such that a wide range of values are reported in the literature across three orders of magnitude (from 10^{-1} pN/nm to 10^{-4} pN/nm) [52, 77, 80]. This range can be attributed to dynamic lipid rearrangements [89], membrane-cytoskeletal interactions [90], and rearrangement of force-generating NMIIA molecules [32]. Our theoretical analyses, supported by experimental measurements, implicitly suggests that for a biconcave RBC, the effective membrane tension should be on the order of 10^{-2} pN/nm.

Our conclusions of non-uniform force density and tension regulation can be used to obtain insight into the effective activity of NMIIA motor domains at any given time. Assuming that a single NMIIA motor domain produces an average force of ~ 1 pN [91], the calculated force densities in Fig. 7B correspond to 178 and 1628 myosin motor domains in the dimple and donut regions, respectively. This means that the force generated by a total $\sim$1,800 active NMIIA motor domains, distributed between the dimple and the donut as we predicted, is sufficient to sustain the biconcave disk shape of an RBC. Previous studies estimated that each mature human RBC contains $\sim$6,000 NMIIA molecules, $\sim$12,000 motor domains [30, 31] and at any given time, roughly 40-50% of these molecules are bound to the cytoskeleton. Our calculations suggest that approximately 30% of these bound NMIIA molecules are active and exerting forces (heterogeneously). It is also possible that the amount of force generated by a single NMIIA motor domain varies due to the stiffness of the membrane cytoskeleton network, the processivity (the duration over which the motor stays attached to actin), and the cross-linking activity of NMIIA myosin filaments [92, 93]. Therefore, further research is required to determine the quantitative relationship between the copy number of NMIIA molecules and their activity, measured by the magnitude of force they exert on the RBC membrane.

The idea of the asymmetrical distribution of the membrane cytoskeleton and its components in the dimple and donut areas of RBCs was initially introduced by Hoffman [94, 95]. Recently, Svetina et al. modeled RBC vol-

13

ume regulation according to permeability of the Piezo1 channel. Based on their simulation results, they found that Piezo1 channels are distributed non-uniformly in a biconcave RBC, tending to localize in the dimple region [96]. They speculated that the simulated localization of Piezo1 channels in the dimple region is controlled by the membrane curvature. It is possible that the RBC membrane curvature and induced tractions [97] can also influence the localization of NMIIA motor proteins, as has been observed in other cell types [15]. Alternatively, a shear-induced Ca^{2+} influx through localized Piezo1 channels could locally activate NMIIA through phosphorylation of the regulatory light chain, leading to enhanced NMIIA binding to F-actin in the dimple and enhanced local contractility at dimple, activating Piezo1 and Ca^{2+} influx in a feed-forward loop. We believe our findings in this work are a motivation for future studies to develop quantitative relationships between the myosin-mediated forces, Ca^{2+} influxes, and the membrane curvature of the cell surface.

We acknowledge that despite the conclusions from our studies, there are some limitations and simplifying assumptions that will need to be revisited for future studies. First, we limited our model to axisymmetric shapes, while RBCs often adopt non-axisymmetric shapes [98]. Future studies will involve simulations without any assumptions of symmetry. Second, we modeled the net effects of NMIIA motor proteins as local forces applied normally to the membrane surface. However, there is evidence that these molecules also exert forces on the membrane surface (tangential to the membrane) and inclusion of these effects may be important in refining our interpretation of tension. Experimental tests probing wether NMIIA activity is non-uniform across the RBC membrane will also give insight into NMIIA density distribution versus activity distribution. And finally, we assumed that the contributions from thermal fluctuations and the deformation of the membrane cytoskeleton are negligible compared to the bending energy [37, 99]. However, for a more general quantitative model, these effects should be considered.

5- Materials and methods

(a) **Immunofluorescence staining of RBCs**. Human peripheral whole blood was collected from healthy human donors into EDTA tubes (BD Diagnostics). 20 μl of whole blood was added to 1 ml of 4% paraformaldehyde (PFA, Electron Microscopy Sciences) in Dulbecco's PBS (DPBS – Gibco), mixed, and incubated at room temperature overnight.

  (i) **NMIIA immunostaining and rhodamine phalloidin staining**. Fixed RBCs were washed three times in DPBS by centrifuging for 5 minutes at 1000 x g, permeabilized in DPBS + 0.3% TX-100 for 10 minutes, and then blocked in 4% BSA, 1% normal goat serum in DPBS (Blocking Buffer, BB) at 4^0C for at least 4 days or up to 1 week before immunostaining. Permeabilized and blocked RBCs were then incubated with rabbit anti-NMIIA motor domain antibody (Abcam ab75590) diluted in BB (1:1000) for 2-3 hours at room temperature, washed two times in BB as above, and then incubated in Alexa-488-conjugated goat anti-rabbit secondary antibody (Life Technologies A11008, diluted 1:1000) mixed with rhodamine-phalloidin (Life Technologies R415, at a final concentration of 130 nM) in BB for 1-2 hr at room temperature, followed by washing three times in BB as above. Stained cells were cytospun onto slides and mounted with ProLongTM Gold mounting medium (Invitrogen) and coverslipped prior to imaging.

  (ii) **Glycophorin A (GPA) immunostaining**. Fixed RBCs were washed three times in DPBS by centrifuging for 5 minutes at 1000 x g, blocked for 1 hour in BB, and stained with FITC-conjugated mouse anti-GPA antibody (BD Pharmingen 559943) for 1 hour at room temperature. GPA-stained RBCs were washed twice in DPBS by centrifugation as above, then cytospun onto glass slides and mounted with ProlongTM Gold and coverslipped prior to imaging.

(b) **Fluorescence microscopy**.

  (i) **RBCs immunostained for NMIIA and rhodamine phalloidin for F-actin**. RBCs were imaged using a Zeiss LSM 880 Airyscan laser scanning confocal microscope with a 63×1.46 NA oil Plan Apo objective. Z-stacks were acquired at a digital zoom of 1.8 and a Z-step size of 0.168 μm.

(ii) **RBCs immunostained for GPA**. RBCs were imaged using a Zeiss LSM 780 laser scanning confocal microscope with a 100×1.4 NA oil Plan Apo objective. Z-stacks were acquired at a digital zoom of 1.0 and a Z-step size of 0.25 μm. To correct for Z-stretch in the images used in this manuscript, the distance between Z-steps was set to 0.18 μm.

(c) **Image analysis**. To correct for Z-stretch in the Airyscan confocal stacks, the distance between Z-steps was set to 0.1 μm. Numbers of NMIIA puncta in whole RBCs, in the dimples, and in the donuts were counted automatically from Airyscan confocal stacks in Volocity (Quorum Technologies) using the "Find Spots" function in the "Measurements" module. The volumes of whole RBCs, the dimples, and the donuts were measured from the rhodamine phalloidin (F-actin) fluorescence in Volocity using the "Find Objects" function, with gaps in staining filled using the "Close" function. RBC height measurements were acquired manually from XZ views of the center of each RBC in Volocity using the line function to measure the distance between the edges of fluorescent F-actin staining signal at the widest and narrowest regions of each RBC.

(d) **Statistical analysis**. Data are presented in dot plots as mean $\pm$ standard deviation (SD), or in scatter plots showing the best-fit line from the linear regression. Differences between the variances of the two samples were detected using F-tests. Differences between means were detected using unpaired t-tests with Welch's correction. When more than one comparison was made, differences between means were detected using one-way ANOVA followed by Tukey's multiple comparisons test. Statistical significance was defined as p < 0.05. Statistical analysis was performed using GraphPad Prism 7.03 software.

Author contributions V.M.F. and P.R. conceived the research. H.A. and A.S.S. carried out the research. H.A., A.S.S., V.M.F., and P.R. wrote the paper. All authors agreed on the contents on the paper.

References

[1] R. Singhvi, A. Kumar, G. P. Lopez, G. N. Stephanopoulos, D. Wang, G. M. Whitesides, and D. E. Ingber, "Engineering cell shape and function," *Science*, vol. 264, no. 5159, pp. 696–698, 1994.

[2] P. Rangamani, A. Lipshtat, E. U. Azeloglu, R. C. Calizo, M. Hu, S. Ghassemi, J. Hone, S. Scarlata, S. R. Neves, and R. Iyengar, "Decoding information in cell shape," *Cell*, vol. 154, no. 6, pp. 1356–1369, 2013.

[3] M. Murrell, P. W. Oakes, M. Lenz, and M. L. Gardel, "Forcing cells into shape: the mechanics of actomyosin contractility," *Nature reviews Molecular cell biology*, vol. 16, no. 8, p. 486, 2015.

[4] E. Paluch, C. Sykes, J. Prost, and M. Bornens, "Dynamic modes of the cortical actomyosin gel during cell locomotion and division," *Trends in cell biology*, vol. 16, no. 1, pp. 5–10, 2006.

[5] G. Salbreux, G. Charras, and E. Paluch, "Actin cortex mechanics and cellular morphogenesis," *Trends in cell biology*, vol. 22, no. 10, pp. 536–545, 2012.

[6] M. Vicente-Manzanares, X. Ma, R. S. Adelstein, and A. R. Horwitz, "Non-muscle myosin ii takes centre stage in cell adhesion and migration," *Nature reviews Molecular cell biology*, vol. 10, no. 11, p. 778, 2009.

[7] S. M. Heissler and D. J. Manstein, "Nonmuscle myosin-2: mix and match," *Cellular and Molecular Life Sciences*, vol. 70, no. 1, pp. 1–21, 2013.

[8] M. A. Conti and R. S. Adelstein, "Nonmuscle myosin ii moves in new directions," *Journal of cell science*, vol. 121, no. 1, pp. 11–18, 2008.

[9] R. Kalluri and R. A. Weinberg, "The basics of epithelial-mesenchymal transition," *The Journal of clinical investigation*, vol. 119, no. 6, pp. 1420–1428, 2009.

[10] S. M. Lyons, E. Alizadeh, J. Mannheimer, K. Schuamberg, J. Castle, B. Schroder, P. Turk, D. Thamm, and A. Prasad, "Changes in cell shape are correlated with metastatic potential in murine and human osteosarcomas," *Biology open*, vol. 5, no. 3, pp. 289–299, 2016.

[11] S. Suresh, J. Spatz, J. Mills, A. Micoulet, M. Dao, C. Lim, M. Beil, and T. Seufferlein, "Connections between single-cell biomechanics and human disease states: gastrointestinal cancer and malaria," *Acta biomaterialia*, vol. 1, no. 1, pp. 15–30, 2005.

[12] L. Da Costa, J. Galimand, O. Fenneteau, and N. Mohandas, "Hereditary spherocytosis, elliptocytosis, and other red cell membrane disorders," *Blood reviews*, vol. 27, no. 4, pp. 167–178, 2013.

[13] M. Diez-Silva, M. Dao, J. Han, C.-T. Lim, and S. Suresh, "Shape and biomechanical characteristics of human red blood cells in health and disease," *MRS bulletin*, vol. 35, no. 5, pp. 382–388, 2010.

[14] A. S. Smith, K. Pal, R. B. Nowak, A. Demenko, C. Zaninetti, L. Da Costa, R. Favier, A. Pecci, and V. M. Fowler, "Myh9-related disease mutations cause abnormal red blood cell morphology through increased myosin-actin binding at the membrane," *American journal of hematology*, 2019.

[15] A. Tousley, M. Iuliano, E. Weisman, E. Sapp, N. Zhang, P. Vodicka, J. Alexander, H. Aviolat, L. Gatune, P. Reeves, *et al.*, "Rac1 activity is modulated by huntingtin and dysregulated in models of huntington's disease," *Journal of Huntington's disease*, no. Preprint, pp. 1–17, 2019.

[16] H. Elliott, R. S. Fischer, K. A. Myers, R. A. Desai, L. Gao, C. S. Chen, R. S. Adelstein, C. M. Waterman, and G. Danuser, "Myosin ii controls cellular branching morphogenesis and migration in three dimensions by minimizing cell-surface curvature," *Nature cell biology*, vol. 17, no. 2, p. 137, 2015.

[17] N. Mohandas and E. Evans, "Mechanical properties of the red cell membrane in relation to molecular structure and genetic defects," *Annual review of biophysics and biomolecular structure*, vol. 23, no. 1, pp. 787–818, 1994.

[18] N. Mohandas and P. G. Gallagher, "Red cell membrane: past, present, and future," *Blood*, vol. 112, no. 10, pp. 3939–3948, 2008.

[19] S. Chien, "Red cell deformability and its relevance to blood flow," *Annual review of physiology*, vol. 49, no. 1, pp. 177–192, 1987.

[20] G. J. Kato, M. H. Steinberg, and M. T. Gladwin, "Intravascular hemolysis and the pathophysiology of sickle cell disease," *The Journal of clinical investigation*, vol. 127, no. 3, pp. 750–760, 2017.

[21] B. M. Cooke, N. Mohandas, and R. L. Coppel, "The malaria-infected red blood cell: structural and functional changes," 2001.

[22] E. S. Zuccala and J. Baum, "Cytoskeletal and membrane remodelling during malaria parasite invasion of the human erythrocyte," *British journal of haematology*, vol. 154, no. 6, pp. 680–689, 2011.

[23] W. Helfrich, "Elastic properties of lipid bilayers: theory and possible experiments," *Zeitschrift für Naturforschung C*, vol. 28, no. 11-12, pp. 693–703, 1973.

[24] P. B. Canham, "The minimum energy of bending as a possible explanation of the biconcave shape of the human red blood cell," *Journal of theoretical biology*, vol. 26, no. 1, pp. 61–81, 1970.

[25] H. Deuling and W. Helfrich, "Red blood cell shapes as explained on the basis of curvature elasticity," *Biophysical journal*, vol. 16, no. 8, pp. 861–868, 1976.

[26] W. Gratzer, "The red cell membrane and its cytoskeleton.," *Biochemical Journal*, vol. 198, no. 1, p. 1, 1981.

[27] V. M. Fowler, "The human erythrocyte plasma membrane: A rosetta stone for decoding membrane–cytoskeleton structure," in *Current topics in membranes*, vol. 72, pp. 39–88, Elsevier, 2013.

[28] D. S. Gokhin and V. M. Fowler, "Feisty filaments: actin dynamics in the red blood cell membrane skeleton," *Current opinion in hematology*, vol. 23, no. 3, p. 206, 2016.

[29] D. E. Discher, "New insights into erythrocyte membrane organization and microelasticity," *Current opinion in hematology*, vol. 7, no. 2, pp. 117–122, 2000.

[30] V. M. Fowler, J. Q. Davis, and V. Bennett, "Human erythrocyte myosin: identification and purification.," *The Journal of cell biology*, vol. 100, no. 1, pp. 47–55, 1985.

[31] A. J. Wong, D. P. Kiehart, and T. D. Pollard, "Myosin from human erythrocytes.," *Journal of Biological Chemistry*, vol. 260, no. 1, pp. 46–49, 1985.

[32] A. S. Smith, R. B. Nowak, S. Zhou, M. Giannetto, D. S. Gokhin, J. Papoin, I. C. Ghiran, L. Blanc, J. Wan, and V. M. Fowler, "Myosin iia interacts with the spectrin-actin membrane skeleton to control red blood cell membrane curvature and deformability," *Proceedings of the National Academy of Sciences*, vol. 115, no. 19, pp. E4377–E4385, 2018.

[33] W. Rawicz, K. Olbrich, T. McIntosh, D. Needham, and E. Evans, "Effect of chain length and unsaturation on elasticity of lipid bilayers," *Biophysical journal*, vol. 79, no. 1, pp. 328–339, 2000.

[34] D. Steigmann, "Fluid films with curvature elasticity," *Archive for Rational Mechanics and Analysis*, vol. 150, no. 2, pp. 127–152, 1999.

[35] P. Rangamani, A. Agrawal, K. K. Mandadapu, G. Oster, and D. J. Steigmann, "Interaction between surface shape and intra-surface viscous flow on lipid membranes," *Biomechanics and modeling in mechanobiology*, vol. 12, no. 4, pp. 833–845, 2013.

[36] H. Alimohamadi, B. Ovryn, and P. Rangamani, "Modeling membrane nanotube morphology: the role of heterogeneity in composition and material properties," *bioRxiv*, p. 373811, 2018.

[37] G. Lim HW, M. Wortis, and R. Mukhopadhyay, "Red blood cell shapes and shape transformations: newtonian mechanics of a composite membrane: sections 2.1–2.4," *Soft Matter: Lipid Bilayers and Red Blood Cells*, vol. 4, pp. 83–139, 2008.

[38] R. Mukhopadhyay, H. G. Lim, and M. Wortis, "Echinocyte shapes: bending, stretching, and shear determine spicule shape and spacing," *Biophysical Journal*, vol. 82, no. 4, pp. 1756–1772, 2002.

[39] C. Picart and D. E. Discher, "Actin protofilament orientation at the erythrocyte membrane," *Biophysical journal*, vol. 77, no. 2, pp. 865–878, 1999.

[40] C. Picart, P. Dalhaimer, and D. E. Discher, "Actin protofilament orientation in deformation of the erythrocyte membrane skeleton," *Biophysical journal*, vol. 79, no. 6, pp. 2987–3000, 2000.

[41] J. T. Jenkins, "The equations of mechanical equilibrium of a model membrane," *SIAM Journal on Applied Mathematics*, vol. 32, no. 4, pp. 755–764, 1977.

[42] J. Jenkins, "Static equilibrium configurations of a model red blood cell," *J. Math. Biol.*, vol. 4, no. 2, pp. 149–169, 1977.

[43] B. K. Pai and H. D. Weymann, "Equilibrium shapes of red blood cells in osmotic swelling," *Journal of biomechanics*, vol. 13, no. 2, pp. 105–112, 1980.

[44] N. Mohandas and J. Chasis, "Red blood cell deformability, membrane material properties and shape: regulation by transmembrane, skeletal and cytosolic proteins and lipids.," in *Seminars in hematology*, vol. 30, pp. 171–192, 1993.

[45] Y. Fung and P. Tong, "Theory of the sphering of red blood cells," *Biophysical journal*, vol. 8, no. 2, pp. 175–198, 1968.

[46] H. Park, S. Lee, M. Ji, K. Kim, Y. Son, S. Jang, and Y. Park, "Measuring cell surface area and deformability of individual human red blood cells over blood storage using quantitative phase imaging," *Scientific reports*, vol. 6, p. 34257, 2016.

[47] J. C. Luke, "A method for the calculation of vesicle shapes," *SIAM Journal on Applied Mathematics*, vol. 42, no. 2, pp. 333–345, 1982.

[48] S. Svetina and B. Žekš, "Membrane bending energy and shape determination of phospholipid vesicles and red blood cells," *European biophysics journal*, vol. 17, no. 2, pp. 101–111, 1989.

[49] P. Rangamani, K. K. Mandadap, and G. Oster, "Protein-induced membrane curvature alters local membrane tension," *Biophysical journal*, vol. 107, no. 3, pp. 751–762, 2014.

[50] A. Agrawal and D. J. Steigmann, "Modeling protein-mediated morphology in biomembranes," *Biomechanics and modeling in mechanobiology*, vol. 8, no. 5, p. 371, 2009.

[51] H. Alimohamadi and P. Rangamani, "Modeling membrane curvature generation due to membrane–protein interactions," *Biomolecules*, vol. 8, no. 4, p. 120, 2018.

[52] R. P. Rand and A. Burton, "Mechanical properties of the red cell membrane: I. membrane stiffness and intracellular pressure," *Biophysical Journal*, vol. 4, no. 2, pp. 115–135, 1964.

[53] P. Canham and A. C. Burton, "Distribution of size and shape in populations of normal human red cells," *Circulation research*, vol. 22, no. 3, pp. 405–422, 1968.

[54] S. Chien, S. Usami, R. J. Dellenback, and C. A. Bryant, "Comparative hemorheology—hematological implications of species differences in blood viscosity," *Biorheology*, vol. 8, no. 1, pp. 35–57, 1971.

[55] E. Evans and Y.-C. Fung, "Improved measurements of the erythrocyte geometry," *Microvascular research*, vol. 4, no. 4, pp. 335–347, 1972.

[56] Y. Fung, W. C. Tsang, and P. Patitucci, "High-resolution data on the geometry of red blood cells," *Biorheology*, vol. 18, no. 3-6, pp. 369–385, 1981.

[57] G. V. Richieri, S. P. Akeson, and H. C. Mel, "Measurement of biophysical properties of red blood cells by resistance pulse spectroscopy: volume, shape, surface area, and deformability," *Journal of biochemical and biophysical methods*, vol. 11, no. 2-3, pp. 117–131, 1985.

[58] O. Linderkamp, E. Friederichs, and H. J. Meiselman, "Mechanical and geometrical properties of density-separated neonatal and adult erythrocytes," *Pediatric research*, vol. 34, no. 5, p. 688, 1993.

[59] K. G. Engström and H. J. Meiselman, "Optical and mathematical corrections of micropipette measurements of red blood cell geometry during anisotonic perifusion," *Cytometry: The Journal of the International Society for Analytical Cytology*, vol. 17, no. 4, pp. 279–286, 1994.

[60] D. Tycko, M. Metz, E. Epstein, and A. Grinbaum, "Flow-cytometric light scattering measurement of red blood cell volume and hemoglobin concentration," *Applied optics*, vol. 24, no. 9, pp. 1355–1365, 1985.

[61] P. Tarasov, M. Yurkin, P. Avrorov, K. Semyanov, A. Hoekstra, and V. Maltsev, "Optics of erythrocytes," in *Optics of Biological Particles*, pp. 243–259, Springer, 2007.

[62] Ö. Ergül, A. Arslan-Ergül, and L. Gürel, "Computational study of scattering from healthy and diseased red blood cells," *Journal of biomedical optics*, vol. 15, no. 4, p. 045004, 2010.

[63] M. Das, B. Das, A. Das, I. Chatterjee, and D. Majumder, "Computational analysis of ultrastructural images of red blood cells," *Journal of Oncology Translational Research*, vol. 1, no. 1, p. 103, 2015.

[64] H. FUNAKI, "Contributions on the shapes of red blood corpuscles," *The Japanese journal of physiology*, vol. 5, pp. 81–92, 1955.

[65] P. W. Kuchel and E. D. Fackerell, "Parametric-equation representation of biconcave erythrocytes," *Bulletin of mathematical biology*, vol. 61, no. 2, pp. 209–220, 1999.

[66] M. A. Yurkin *et al.*, *Discrete dipole simulations of light scattering by blood cells*. Universiteit van Amsterdam [Host], 2007.

[67] A. G. Borovoi, E. I. Naats, and U. G. Oppel, "Scattering of light by a red blood cell," *Journal of biomedical optics*, vol. 3, no. 3, pp. 364–373, 1998.

[68] L. Bi and P. Yang, "Modeling of light scattering by biconcave and deformed red blood cells with the invariant imbedding t-matrix method," *Journal of biomedical optics*, vol. 18, no. 5, p. 055001, 2013.

[69] M. A. Yurkin, K. A. Semyanov, P. A. Tarasov, A. V. Chernyshev, A. G. Hoekstra, and V. P. Maltsev, "Experimental and theoretical study of light scattering by individual mature red blood cells by use of scanning flow cytometry and a discrete dipole approximation," *Applied Optics*, vol. 44, no. 25, pp. 5249–5256, 2005.

[70] J. Lyu, P. G. Chen, G. Boedec, M. Leonetti, and M. Jaeger, "Hybrid continuum–coarse-grained modeling of erythrocytes," *Comptes Rendus Mécanique*, vol. 346, no. 6, pp. 439–448, 2018.

[71] H. Deuling and W. Helfrich, "The curvature elasticity of fluid membranes: a catalogue of vesicle shapes," *Journal de Physique*, vol. 37, no. 11, pp. 1335–1345, 1976.

[72] E. A. Evans, *Mechanics and Thermodynamics of Biomembranes: 0*. CRC press, 2018.

[73] P. Zarda, S. Chien, and R. Skalak, "Elastic deformations of red blood cells," *Journal of biomechanics*, vol. 10, no. 4, pp. 211–221, 1977.

[74] P. Zarda, S. Chien, and R. Skalak, "Sphering and formation of red blood cells," in *Biomechanics Symposium. R. Skalak and RM Nerem, editors. AMD*, vol. 10, p. 49, 1975.

[75] P. R. Zarda, *Large deformations of an elastic shell in a viscous fluid*. UMI Dissertation Services, 2004.

[76] A. H. Lewis and J. Grandl, "Mechanical sensitivity of piezo1 ion channels can be tuned by cellular membrane tension," *Elife*, vol. 4, p. e12088, 2015.

[77] J. Evans, W. Gratzer, N. Mohandas, K. Parker, and J. Sleep, "Fluctuations of the red blood cell membrane: relation to mechanical properties and lack of atp dependence," *Biophysical journal*, vol. 94, no. 10, pp. 4134–4144, 2008.

[78] Z. Shi, Z. T. Graber, T. Baumgart, H. A. Stone, and A. E. Cohen, "Cell membranes resist flow," *Cell*, vol. 175, no. 7, pp. 1769–1779, 2018.

[79] J. Huff, "The airyscan detector from zeiss: confocal imaging with improved signal-to-noise ratio and super-resolution," *Nature methods*, vol. 12, no. 12, 2015.

[80] G. Popescu, T. Ikeda, K. Goda, C. A. Best-Popescu, M. Laposata, S. Manley, R. R. Dasari, K. Badizadegan, and M. S. Feld, "Optical measurement of cell membrane tension," *Physical review letters*, vol. 97, no. 21, p. 218101, 2006.

[81] A. Diz-Muñoz, D. A. Fletcher, and O. D. Weiner, "Use the force: membrane tension as an organizer of cell shape and motility," *Trends in cell biology*, vol. 23, no. 2, pp. 47–53, 2013.

[82] D. Hodgkin and J. Lister, "Xxvi. notice of some miscroscopic observations of the blood and animal tissues," *The Philosophical Magazine*, vol. 2, no. 8, pp. 130–138, 1827.

[83] D. Kuzman, S. Svetina, R. Waugh, and B. Žekš, "Elastic properties of the red blood cell membrane that determine echinocyte deformability," *European Biophysics Journal*, vol. 33, no. 1, pp. 1–15, 2004.

[84] Z. Peng, X. Li, I. V. Pivkin, M. Dao, G. E. Karniadakis, and S. Suresh, "Lipid bilayer and cytoskeletal interactions in a red blood cell," *Proceedings of the National Academy of Sciences*, vol. 110, no. 33, pp. 13356–13361, 2013.

[85] Z. Peng, R. J. Asaro, and Q. Zhu, "Multiscale simulation of erythrocyte membranes," *Physical Review E*, vol. 81, no. 3, p. 031904, 2010.

[86] I. V. Pivkin, Z. Peng, G. E. Karniadakis, P. A. Buffet, M. Dao, and S. Suresh, "Biomechanics of red blood cells in human spleen and consequences for physiology and disease," *Proceedings of the National Academy of Sciences*, vol. 113, no. 28, pp. 7804–7809, 2016.

[87] Z. Peng, A. Mashayekh, and Q. Zhu, "Erythrocyte responses in low-shear-rate flows: effects of non-biconcave stress-free state in the cytoskeleton," *Journal of Fluid Mechanics*, vol. 742, pp. 96–118, 2014.

[88] A. Colom, E. Derivery, S. Soleimanpour, C. Tomba, M. Dal Molin, N. Sakai, M. González-Gaitán, S. Matile, and A. Roux, "A fluorescent membrane tension probe," *Nature chemistry*, vol. 10, no. 11, p. 1118, 2018.

[89] F. Jähnig, "What is the surface tension of a lipid bilayer membrane?," *Biophysical journal*, vol. 71, no. 3, pp. 1348–1349, 1996.

[90] M. Sheetz, "Membrane skeletal dynamics: role in modulation of red cell deformability, mobility of transmembrane proteins, and shape.," in *Seminars in hematology*, vol. 20, pp. 175–188, 1983.

[91] Y. Takagi, R. E. Farrow, N. Billington, A. Nagy, C. Batters, Y. Yang, J. R. Sellers, and J. E. Molloy, "Myosin-10 produces its power-stroke in two phases and moves processively along a single actin filament under low load," *Proceedings of the National Academy of Sciences*, vol. 111, no. 18, pp. E1833–E1842, 2014.

[92] N. Hundt, W. Steffen, S. Pathan-Chhatbar, M. H. Taft, and D. J. Manstein, "Load-dependent modulation of non-muscle myosin-2a function by tropomyosin 4.2," *Scientific reports*, vol. 6, p. 20554, 2016.

[93] M. F. Norstrom, P. A. Smithback, and R. S. Rock, "Unconventional processive mechanics of non-muscle myosin iib," *Journal of Biological Chemistry*, vol. 285, no. 34, pp. 26326–26334, 2010.

[94] J. F. Hoffman, "Biconcave shape of human red-blood-cell ghosts relies on density differences between the rim and dimple of the ghost's plasma membrane," *Proceedings of the National Academy of Sciences*, vol. 113, no. 51, pp. 14847–14851, 2016.

[95] J. F. Hoffman, "Evidence that asymmetry of the membrane/cytoskeletal complex in human red blood cell ghosts is responsible for their biconcave shape," *Proceedings of the National Academy of Sciences*, vol. 115, no. 7, pp. 1641–1645, 2018.

[96] S. Svetina, T. Š. Kebe, and B. Božič, "A model of piezo1-based regulation of red blood cell volume," *Biophysical journal*, vol. 116, no. 1, pp. 151–164, 2019.

[97] H. Alimohamadi, R. Vasan, J. E. Hassinger, J. C. Stachowiak, and P. Rangamani, "The role of traction in membrane curvature generation," *Molecular biology of the cell*, vol. 29, no. 16, pp. 2024–2035, 2018.

[98] B. Kaoui, G. Biros, and C. Misbah, "Why do red blood cells have asymmetric shapes even in a symmetric flow?," *Physical review letters*, vol. 103, no. 18, p. 188101, 2009.

[99] S. Svetina, G. Kokot, T. Š. Kebe, B. Žekš, and R. E. Waugh, "A novel strain energy relationship for red blood cell membrane skeleton based on spectrin stiffness and its application to micropipette deformation," *Biomechanics and modeling in mechanobiology*, vol. 15, no. 3, pp. 745–758, 2016.